



BNL-75212-2005-JA

**HIERARCHICAL APPROACH TO MODEL MULTILAYER
COLLOIDAL DEPOSITION IN POROUS MEDIA**

P. Kulkarni, R. Sureshkumar, and P. Biswas

*Published in
Environ. Sci. Technol. 39, 6361-6370 (2005)*

September 2005

Environmental Sciences Dept./Atmospheric Sciences Div.

Brookhaven National Laboratory

P.O. Box 5000
Upton, NY 11973-5000
www.bnl.gov

Hierarchical Approach to Model Multilayer Colloidal Deposition in Porous Media[†]

PRAMOD KULKARNI,^{‡,§}
R. SURESHKUMAR,^{||} AND
PRATIM BISWAS^{*,§,||}

Brookhaven National Laboratory, P.O. Box 5000, Building 815E, Upton, New York 11973, and Environmental Engineering Science and Department of Chemical Engineering, Washington University in Saint Louis, Campus Box 1180, Saint Louis, Missouri 63130

Particle deposition is important in many environmental systems such as water and wastewater filtration, air pollution control, subsurface transport, biofilm formation and fouling, and thin film synthesis for use in remediation technologies. While continuum-level models have been developed to predict deposition dynamics in these systems, these models fail to explain transient dynamics of multilayer deposition from a mechanistic viewpoint. In this work, a multiscale approach has been developed to predict multiple layer irreversible colloidal deposition in the presence of interparticle electrostatic and van der Waals interactions in porous media. The approach combines the kinetic information obtained from the mesoscopic stochastic simulations of particle deposition with the macroscopic conservation equation describing colloidal transport. Sequential Brownian dynamics simulations are first performed by accounting for particle–particle (P–P) and particle–surface (P–S) interactions, and multilayered particle deposits are obtained. The available surface function quantifying the deposition kinetics is then obtained from the deposit microstructure. Deposition dynamics are studied at different ionic strengths and particle potentials that control the range and magnitude of interparticle interactions. Simulation results showed that the microstructure of the particle deposits formed under the influence of P–P and P–S electrostatic interactions exhibited significant variations with respect to ionic strength and could be qualitatively explained by the interplay between the repulsive and attractive P–P and P–S interaction forces. The available surface function also varied significantly as a function of ionic strength. This basic understanding of the deposition dynamics at the mesoscale was then combined with the continuum-level transport equations to predict particle breakthrough curves in porous media. The approach is capable of capturing transient features of deposition dynamics, as

demonstrated by the good agreement between the model predictions and the experimental observations.

Introduction

Transport of particles toward a solid–liquid or a gas–solid interface, often referred to as deposition, is of importance in many environmental systems such as water and wastewater filtration, air pollution control devices, subsurface contaminant transport, biofilm formation and fouling, and nanostructured coatings/films synthesis for use in remediation technologies. In light of these applications, development of theoretical models that accurately capture the dynamical behavior under a variety of operating conditions is important. Continuum-level models do not accurately predict deposition dynamics as they do not account for the varying and evolving structure of the deposit. Colloidal deposition on collector surfaces is often irreversible and has been the subject of numerous theoretical and experimental studies (1), although the primary focus has been on convective and/or diffusional deposition leading to monolayer formation on the adsorption surface (2–8). Monolayer deposition theories (wherein incoming particles can only deposit on the unoccupied locations on the surface and where deposition stops, due to electrostatic repulsion, after achieving the saturation coverage in the first layer) have been used to predict deposition kinetics. The most widely used model of irreversible monolayer deposition of hard spherical particles in the dilute limit is the random sequential adsorption (RSA) model (2, 9, 10). Deposition kinetics in RSA has been widely studied (2, 4, 8, 11, 12) by using a pseudo timescale obtained from the number of deposition attempts.

In many environmental processes, the suspensions are not always stable due to high ionic strength or low particle potential, and the assumption of monolayer formation is not valid; deposition of incoming particles onto already deposited particles is feasible. For example, in porous media, such as a filter bed, the rate of deposition of particles often increases with time, a phenomenon referred to as “filter ripening” (13–16). In such systems the deposited particles form multilayered fractal structures that increase the available surface area, and hence the net deposition rate (14). Furthermore, the retained particles on the surface can significantly influence the flux on depositing particles through short- or long-ranged electrostatic interactions. Thus, in contrast to monolayer deposition, the rate of multilayer deposit formation depends not only on interparticle interactions but also on the morphology of the deposit structure.

Multilayer deposition in porous media has mainly been described phenomenologically by Omelia and Ali (13). Privman et al. (17) presented a mean field theory for multilayer deposition in packed beds. They formulated their model along the lines of monolayer theories and included a parameter characterizing deposition probability on retained particles. Lubachevsky et al. (18) used computer simulations to study morphology of particle deposits formed under ballistic deposition. Wiesner and co-workers (19–21) have investigated the relationship between transport mechanisms, deposit morphology, and pressure loss in porous media. Recently, Kulkarni et al. (22) studied the role of interparticle interactions on morphology of colloidal deposits resulting from diffusional deposition on a one-dimensional substrate. They studied variation of coverage in different layers as a function of particle potential and electrolyte concentration using a multiscale simulation approach with lattice-based simulations for deposition onto a 1-D surface.

[†] This paper is part of the Charles O’Melia tribute issue.

* Corresponding author telephone: (314)935-5482; fax: 314-935-5464; e-mail: Pratim.Biswas@wustl.edu.

[‡] Brookhaven National Laboratory.

[§] Environmental Engineering Science, Washington University in Saint Louis.

^{||} Department of Chemical Engineering, Washington University in Saint Louis.

Experimental studies on deposition provide sufficient evidence of existence of multilayers under electrostatically or hydrodynamically favorable conditions (1, 16, 23). Ryde et al. (1) studied the effect of electrolyte concentration on deposition of spherical hematite particles on spherical glass collectors in a packed column to investigate the influence of colloidal stability on multilayer deposition. They found that the multilayer model developed by Privman et al. (17) could explain the trends in experimental data, whereas the monolayer model failed to do so. Song and Elimelech (15) have investigated the role of retained particles on deposition rates in porous media. Liu et al. (16) examined the role of electrolyte concentration on deposition dynamics. Kuhn et al. (23) studied transport of iron oxide colloids in packed quartz sand media at varying ionic strengths and clearly observed multilayer deposition at high ionic strengths.

Since particle deposition is an inherently dynamical process exhibiting variable kinetics during the course of deposition, the concept of available surface (or blocking) function has been used to capture the range of kinetic behaviors including initial rates and long time asymptotic behavior (2, 5, 24). The available surface function essentially characterizes the probability of a particle depositing on a bare collector surface and is a function of fraction of collector area occupied by deposited particles. Schaaf and Talbot (24) developed an expression for available surface function based on a virial expansion of excluded area effects to the third order in coverage, valid for low to moderate coverage values. Adamczyk et al. developed a more general expression for soft spheres by using the “blocking parameter” (25). Johnson and Elimelech (7) have used a Langmuir- and RSA-based dynamical blocking function to describe monolayer deposition in porous media. They used experimentally estimated saturation coverages in conjunction with the RSA- and Langmuirian-type blocking functions to predict particle breakthrough curves in porous media. A RSA-type blocking function was found to capture the monolayer deposition dynamics more accurately as compared to Langmuirian. They also observed that at high ionic strength, when deposition was possibly multilayered, the RSA blocking function could not capture the dynamics satisfactorily. Recently, Magan and Sureshkumar (32) have developed an efficient multiscale algorithm for irreversible monolayer deposition. They combined Brownian dynamics simulations to evaluate particle trajectories with the solution of the continuum-level conservation law for particle concentration to help reduce the CPU time. The blocking function was found to be between the asymptotic results of the RSA and ballistic deposition values. These studies dealt with monolayer systems, in which the deposition flux decreased with time due to interparticle repulsive interactions. In contrast to monolayer deposition, multilayer systems are much more complex since the kinetics depend not only on interparticle interactions but also on the fractal morphology of the deposit. In an earlier work, the relationship between deposition mechanism and resulting morphology in the presence of interparticle interactions in multilayer deposition was investigated (22). Lattice based Monte Carlo simulations were performed to understand the influence of range and magnitude of electrostatic interactions on microstructure of deposits formed on a 1-D surface (22). The study revealed the importance of accounting for P–P and P–S interactions in the particle deposition processes.

In this paper, the previous work (22) is extended to a generalized 2-D deposition surface by combining a basic understanding of deposition dynamics obtained from mesoscale stochastic simulations with the solution of continuum-level conservation laws to predict the transient features of deposition dynamics. This approach incorporates the relevant dynamical information about the colloidal deposition process at the mesoscale obtained from Brownian dynamics simula-

tions into the continuum-level particle transport equations to predict breakthrough curves in porous media. Kinetics of coverage in different layers were then used to develop an expression for the available surface function for the entire deposit. The available surface function for the entire deposit is then used to predict macroscopic deposition flux in porous media.

Theory

Irreversible colloidal deposition dynamics in a packed column of spherical collectors has been traditionally modeled using the convection–diffusion equation for macroscopic particle concentration in the porous medium, coupled with a kinetic equation describing monolayer deposition onto the collector surface (7, 17):

$$\frac{\partial C}{\partial t} = D_{\text{eff}} \frac{\partial^2 C}{\partial Z^2} - v_p \frac{\partial C}{\partial Z} - f k_{\text{dep}} \Phi(\theta) C \quad (1a)$$

$$\frac{\partial \theta}{\partial t} = \Phi(\theta) \pi a^2 k_{\text{dep}} C \quad (1b)$$

where C is the number concentration of colloidal particles in the column at time t at the vertical spatial coordinate Z , D_{eff} is the hydrodynamic diffusion coefficient of particles, v_p is the interstitial particle velocity, $\Phi(\theta)$ is the blocking function, k_{dep} is the particle transfer coefficient, a is the particle radius, θ is the surface coverage, and f is the specific surface area of the porous medium in a cylindrical geometry given by

$$f = \frac{3(1 - \epsilon)}{\epsilon a_c} \quad (1c)$$

where ϵ is the porosity of packed bed and a_c is the collector radius. Typically the Peclet number ($v_p l_z / D_{\text{eff}}$) is of the order of $\sim 10^4 - 10^6$ where l_z is a typical length scale in the z direction, taken as collector radius a_c ; and particle diffusion plays only a minor role in axial transport of particles (17). Neglecting diffusion and applying a splitting technique as defined in Privman et al. (17), the above equations are reduced to

$$\frac{\partial C}{\partial X} + f \Phi(\theta) k_{\text{dep}} C = 0 \quad (2a)$$

$$\frac{\partial \theta}{\partial \tau} - \Phi(\theta) \pi a^2 k_{\text{dep}} C = 0 \quad (2b)$$

where

$$X = \frac{Z}{v_p} \quad (2c)$$

$$\tau = t - \frac{Z}{v_p} \quad (2d)$$

with the initial and boundary conditions as

$$C(X, 0) = 0 \quad (2e)$$

$$C(0, \tau > 0) = C_0 \quad (2f)$$

$$\theta(X, 0) = 0 \quad (2g)$$

Note that eq 2a assumes that the colloidal concentration is at steady state. This implies that $v_p / k_{\text{dep}} \gg 1$. This assumption is justifiable since this ratio is typically of the order of $10^2 - 10^3$. To solve the above set of equations, expression for $\Phi(\theta)$ should be known a priori. For monolayer deposition $\Phi(\theta)$ is usually based on either a Langmuirian model:

$$\Phi(\theta) = \left(1 - \frac{\theta}{\theta^{\max}}\right) \quad (3)$$

or RSA (24):

$$\Phi(\theta) = 1 - 4\theta + \frac{6\sqrt{3}}{\pi}\theta^2 + \left(\frac{40}{\pi\sqrt{3}} - \frac{176}{3\pi^2}\right)\theta^3 \quad (4a)$$

where θ^{\max} is monolayer saturation coverage on the surface. $\Phi(\theta)$ can be thus interpreted as the probability of particle deposition on a bare collector surface at a given value of θ . Schaaf and Talbot (24) derived eq 4a based on the RSA simulations for non-interacting hard-spheres where coverage approaches hard-sphere jamming limit (θ_{∞}). The approach incorporates excluded area effects arising from finite size of particles in monolayer deposition. For interacting soft spheres, Adamczyk et al. (25) modified eq 4a:

$$\Phi(\theta) = 1 - 4(\theta \cdot B\theta_{\infty}) + \frac{6\sqrt{3}}{\pi}(\theta \cdot B\theta_{\infty})^2 + \left(\frac{40}{\pi\sqrt{3}} - \frac{176}{3\pi^2}\right)(\theta \cdot B\theta_{\infty})^3 \quad (4b)$$

where B is the blocking parameter and is defined as the inverse of maximum surface coverage, θ^{\max} . However, in case of multilayer deposition, since particles can deposit not only on the nascent collector surface but also on the already

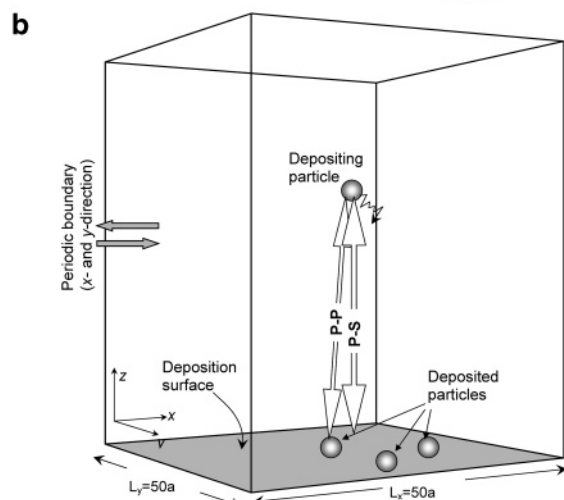
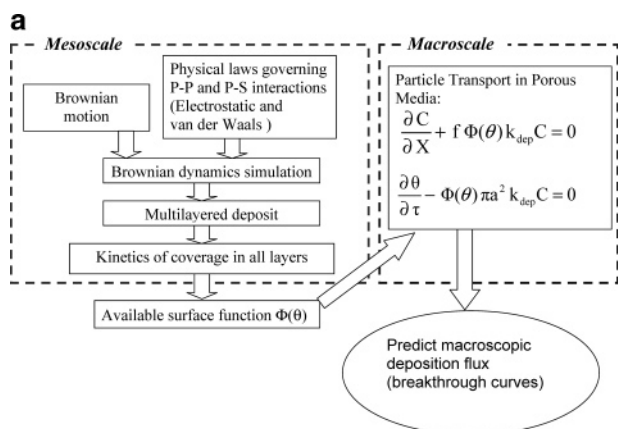


FIGURE 1. (a) Approach used for predicting particle deposition flux in porous media in this work. (b) Box used in simulations. Deposition surface was $50a \times 50a$. The height of the box was increased with the growing deposit. Periodic boundary conditions were used in x- and y-direction. Electrostatic and van der Waals interactions between particle–particle and particle–surface were considered.

retained ones, the deposition dynamics are different and monolayer blocking functions cannot be used.

In this paper a multiscale theoretical framework based on mesoscopic simulations to obtain the available surface function for the multilayer deposition case is developed. Figure 1a outlines the approach used in this work. Brownian dynamics simulations are first performed, incorporating particle diffusion and interparticle P–P and P–S interactions, to obtain a multilayered fractal deposit. Coverage kinetics in the different layers are obtained from the simulation and used to get information on the available surface function. The available surface function is then used to predict macroscopic deposition flux in porous media by the solution of eq 2.

Simulation Approach

Formulation. A semi-infinite region bounded by a 2-D deposition surface is considered as shown in Figure 1b. The fluid in the region (water) is assumed to be quiescent (no flow). The particles were assumed monodisperse with radius, a . The suspension is assumed sufficiently dilute so that interactions between particles in the bulk (not deposited on the surface) are negligible. The thermal energy of the system is characterized by kT , where k is the Boltzmann's constant and T is the temperature of solvent medium with dielectric permittivity ϵ_D . Particles are assumed to be Brownian with a constant self-diffusion coefficient D . The particles that approach the surface interact with other particles deposited on the surface (P–P) and with the nascent deposition surface (P–S) through the following electric double layer (EDL) and van der Waals (VDW) forces:

$$\hat{F}_{\text{pp}}^{\text{EDL}} = Y_{\text{pp}} \left(\frac{(\kappa r_{\text{pp}} + 1)a^2}{r_{\text{pp}}^2} e^{2\kappa a - \kappa r_{\text{pp}}} \right) \hat{e}_{r_{\text{pp}}} \quad (5)$$

$$\hat{F}_{\text{ps}}^{\text{EDL}} = Y_{\text{ps}} (\kappa a e^{-\kappa \delta_{\text{ps}}}) \hat{e}_z \quad (6)$$

$$\hat{F}_{\text{pp}}^{\text{VDW}} = -\frac{A_{\text{pp}}}{3a} \left(\frac{2r_{\text{pp}}}{(r_{\text{pp}}^2 - 4)^2} + \frac{2}{r_{\text{pp}}^3} - \frac{r_{\text{pp}}}{(r_{\text{pp}}^2 - 4)} + \frac{1}{r_{\text{pp}}} \right) \hat{e}_{r_{\text{pp}}} \quad (7)$$

$$\hat{F}_{\text{ps}}^{\text{VDW}} = -\frac{A_{\text{ps}}}{6a} \left(\frac{1}{\delta_{\text{ps}}^2} + \frac{1}{(\delta_{\text{ps}} + 2)^2} - \frac{1}{\delta_{\text{ps}}} + \frac{1}{\delta_{\text{ps}} + 2} \right) \hat{e}_z \quad (8)$$

where Y_{pp} and Y_{ps} are Yukawa coefficients derived from a linear superposition approximation. Expressions for the far field potential provided by Sader (33) were used to derive the Yukawa coefficients Y_{pp} and Y_{ps} :

$$Y_{\text{pp}} = 4\pi\epsilon_D \left(\frac{kT}{e} \right)^2 \left(\frac{4\kappa a \lambda \omega + \Psi_p}{\kappa a \omega + 1} \right)^2 \quad (9)$$

$$Y_{\text{ps}} = 4\pi\epsilon_D \left(\frac{kT}{e} \right)^2 \left(\frac{4\kappa a \lambda \omega + \Psi_p}{\kappa a \omega + 1} \right) \left(4 \tanh\left(\frac{\Psi_s}{4}\right) \right) \quad (10)$$

$$\lambda = \tanh\left(\frac{\Psi_p}{4}\right) \quad (11)$$

$$\omega = \tanh\left(\frac{\Psi_p - 4\lambda}{2\lambda^3}\right) \quad (12)$$

where $\hat{F}_{\text{pp}}^{\text{EDL}}$ and $\hat{F}_{\text{ps}}^{\text{EDL}}$ are the electric double-layer forces, and $\hat{F}_{\text{ps}}^{\text{VDW}}$ and $\hat{F}_{\text{pp}}^{\text{VDW}}$ are the van der Waals forces between the particle and surface and particle and particle respectively, \hat{e}_z and $\hat{e}_{r_{\text{pp}}}$ are unit vectors along the z direction and along the line joining the particle centers respectively, r_{pp} is the

dimensionless (with respect to a) center-to-center interparticle distance, δ_{ps} and δ_{pp} are dimensionless (with respect to a) surface-to-surface separation distance between P–S and P–P, Ψ_p and Ψ_s are particle and surface potentials (assumed to be constant), κ is the inverse Debye length, and A_{pp} and A_{ps} are Hamaker constants for P–P and P–S interaction in water. It should be noted that the z coordinate in the simulations is different from the Z coordinate at macroscale, which denotes the axial distance in the packed column. The particle trajectory was computed using the Langevin equation following approach outlined by Ermak and Yeh (26) and Ermak (27):

$$\hat{r}(t + \delta t) = \hat{r}(t) + \frac{D}{kT} \hat{F}_{\text{ext}}(t) \delta t + \delta \hat{r}_G \quad (13)$$

where $\hat{r}(t + \delta t)$ is position vector of particle center at time $(t + \delta t)$, $\hat{r}(t)$ is position vector at time t , $\hat{F}_{\text{ext}}(t)$ is a resultant force vector due to all external forces acting on the particle, and $\delta \hat{r}_G$ is Gaussian random displacement due to diffusivity D of the particle and is chosen independently from a Gaussian distribution with a zero mean and variance equal to $\langle (\delta \hat{r}_G)^2 \rangle = 2D \delta t$.

Numerical Algorithm. The motion of the particle is simulated in a box bounded by a two-dimensional deposition surface of length L_x , width L_y , and vertical extent L_z as shown in Figure 1b. The box is periodic in the x - and y -directions. The deposition surface is placed at $z = 0$, so that centers of particles have a minimum z coordinate of a . The particles are sequentially released from the top boundary $z = L_z$; the x - and y -coordinate of the particle is chosen randomly using a uniform random number generator. The particle is moved from one point to the other in predetermined time steps, δt , using the algorithm given by eq 13. δt is chosen such that the total displacement of a particle in δt is smaller than the smallest interaction length scale. The deterministic displacement in each of x -, y -, and z -directions is obtained from the total external force acting on the particle. The total external force is computed by summing over all P–P and P–S van der Waals interactions. The random displacement in each direction, δr_G , is computed by generating Gaussian random numbers. After each move, all interparticle distances, P–P and P–S forces are updated. To reduce the CPU time, the P–P and P–S interactions are considered only when they occur within a cutoff radius $R_{\text{cut}} = a + 4/\kappa$ from the particle center. A particle is irreversibly deposited when the particle is in physical contact with either the surface or another particle. The next particle is released from the top boundary only after the previous particle has deposited. This sequential release of particles is an adequate representation of a dilute suspension (28). When the particle moves out of the sidewalls of the box, periodic boundary conditions are invoked. The total time taken by each particle to deposit is recorded. The final height of the deposit is much smaller than total height L_z of the box.

Simulation Parameters. Simulations were performed with spherical particles. The typical box sizes used were $50a$ in the x -, y -, and z -directions. The Hamaker constants, A_{ps} and A_{pp} values, are taken to be 1×10^{-20} J. The distance z of layer n from the deposition surface was given by:

$$z \equiv (2n - 1)a \quad (14)$$

Layers are defined as planes above the deposition surface, spaced $2a$ apart from each other. This representation allows one to visualize the multilayered deposit as a 3-D domain consisting of many deposition planes, one above the other, in which particles deposit. The dimensionless mean coverage in the n th layer (θ_n) was defined as:

$$\theta_n = \frac{\pi a^2 N_n}{L_x L_y} \quad (15)$$

where N_n is the number of particles whose z coordinates lie in $[2(n - 1)a, 2na]$. Hence, θ_n represents the area occupied by all the particles in the n th layer and is a measure of local density in the particle deposit. A particle is assumed to belong to the n th layer as long as its center lies between $2(n - 1)a$ and $2n$, irrespective of the contact point with the previously deposited particle (line joining centers of two contacting particles is not necessarily vertical). The fractal dimension (D_f) of the deposit was obtained from the following scaling law (29):

$$\theta_n \propto z^{-\alpha} \quad (16)$$

where θ_n is given by eq 15, and α is a fractal or Hausdorff codimensionality (29) given by:

$$\alpha = d - D_f \quad (17)$$

where d is the embedding Euclidean dimension of the physical space ($d = 3$ in this study), and D_f is fractal dimensionality of the deposit. D_f is thus obtained from the density variation with z , using eqs 16 and 17.

Results and Discussion

Simulations were first performed with particles diffusing under pure Brownian motion (pure diffusional deposition, no interactions considered). Results were validated with those from large-scale lattice-based diffusion-limited deposition studies (29). Table 1 shows fractal dimensions of fully grown particle deposits for three particle radii. The fractal dimensions, averaged over eight independent simulations, were 2.52, 2.54, and 2.50 for $a = 5$, 30, and 50 nm particles, respectively. These values agree well with lattice-based DLA value of 2.5 reported by Meakin (29) and thus provide an independent confirmation of the deposit generation code used in this work.

Variation of Coverage (θ_n) in Different Layers. Figure 2a shows a deposit obtained from pure diffusional deposition of 30 nm particles. The deposit contains 800 particles and has a fractal dimension of 2.54. Coverage in all the layers was computed according to eq 15 and was monitored as a function of time. Figure 2b shows the variation of coverage in different layers as a function of total coverage $\theta = (\sum_{n=1}^N \theta_n)$. As shown in the figure, coverage in each layer gradually increases to reach saturation value of θ_n^{max} . For layers 2 and above, variation of θ_n could be accurately described by a sigmoidal saturation function:

$$\theta_{n \geq 2}(\theta) = \frac{\theta_n^{\text{max}}}{1 + \exp[-\varphi_n(\theta - \theta_n^0)]} \quad (18)$$

The variation of the surface coverage on the deposition surface ($\theta_{n=1}$) with total coverage, however, was qualitatively different and monotonically increased approaching θ_1^{max}

TABLE 1. Fractal Dimension of Colloidal Deposits Obtained by Pure Diffusional Deposition

a (nm)	fractal dimension (D_f) ^a
5	2.52 (4.1)
30	2.54 (5.1)
50	2.50 (2.5)
lattice-based DLA (29)	2.50 (2.8)

^a Numbers in parentheses indicate % relative standard deviation.

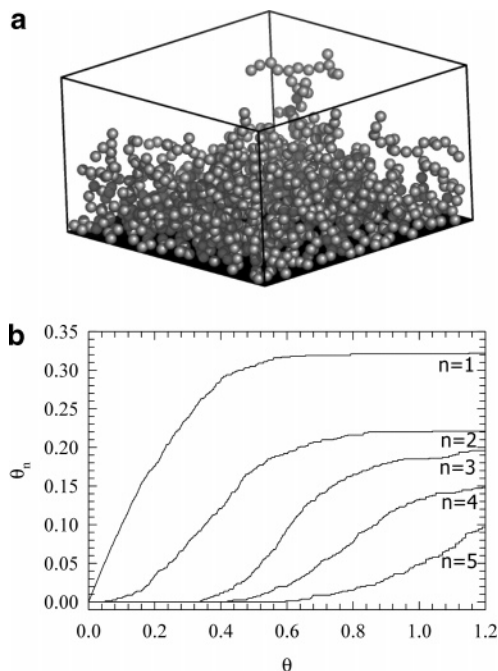


FIGURE 2. (a) Morphology of colloidal deposit obtained after depositing 800 particles. (b) Variation of coverage in different layers as a function of θ ($\theta = \sum_{n=1}^N \theta_n$).

TABLE 2. Regression Parameters (eqs 18 and 19) for Variation of Coverage in the First Few Layers for $\Psi_p = 15$ mV, $\Psi_s = -50$ mV, $\kappa a = 1$

layer, n	θ_1^{\max}	b	γ	R^2 (%)
1	0.3296	0.3296	4.528	98.17

layer, n	θ_n^{\max}	φ_n	θ_n^0	R^2 (%)
2	0.2079	10.6383	0.3851	99.99
3	0.1850	11.8036	0.6028	99.92
4	0.1568	9.3897	0.7738	99.85
5	0.1224	9.4162	0.8934	99.64
6	0.0867	9.3284	1.0020	99.75
7	0.0768	10.3413	1.0760	98.58

asymptotically. Variation of $\theta_{n=1}$ could be accurately described by

$$\theta_{n=1}(\theta) = \theta_1^{\max} - b \exp(-\gamma\theta) \quad (19)$$

where φ_n , θ_n^0 , b , and γ are constants that depend on the layer and characterize the kinetics of variation in coverage in that layer. All these parameters along with the maximum coverage in each layer can be directly obtained from the simulations. Table 2 shows values of φ_n , θ_n^0 , b , and γ for one such case where $\Psi_p = 15$ mV, $\Psi_s = -50$ mV, and $\kappa a = 1$. Table 2 also shows the R^2 statistic for all fits indicating that eqs 18 and 19 accurately describe the variation of coverage. This information can then be used to describe deposition kinetics as described below.

Deposition Kinetics in the Absence of Interactions. The flux of colloidal particles depositing irreversibly on solid surfaces can be written as (5, 8):

$$J(\theta) \equiv \Phi(\theta)k_{\text{dep}}C = \Phi(\theta)J_0 \quad (20)$$

where C is the bulk colloidal concentration far away from the deposition surface, k_{dep} is particle transfer coefficient (analogous to mass transfer coefficient), $\Phi(\theta)$ is available

surface function or dynamic blocking function, J_0 is the incident macroscopic flux from particle transport (available from mass transport with a perfect sink at the surface), and $J(\theta)$ is the actual flux on the surface and may be different from J_0 depending on the nature of electrostatic or hydrodynamic interactions. Thus $\Phi(\theta)$ is simply ratio of actual flux $J(\theta)$ to incident flux J_0 . In case of multilayer deposition, however, the total actual flux $J(\theta)$ on the deposition surface can be written as a sum of flux in n different layers:

$$J(\theta) = \sum_{n=1}^N J_n(\theta) \quad (21)$$

Defining total flux $J(\theta)$ as

$$J(\theta) = \sum_{n=1}^N J_n(\theta) = J_0 \sum_{n=1}^N \Phi_n(\theta) \quad (22)$$

where $\Phi_n(\theta)$ is the available surface function for each layer, and N is the number of layers over which the summation is carried out. $\Phi_n(\theta)$ is thus an indicator function that dictates the probability of particle depositing in the n th layer and will be referred to as available surface function. Expressions for $\Phi_n(\theta)$ can be derived from the kinetics of coverage (θ_n) in n layers as follows. By definition (eq 22), available surface function is ratio of actual flux to J_0 :

$$\Phi_n(\theta) = \frac{J_n(\theta)}{J_0} \quad (23a)$$

However, the actual flux in the n th layer (J_n) is equal to the rate of change of coverage (θ_n) in that layer:

$$J_n(\theta) = \frac{1}{\pi a^2} \frac{\partial \theta_n(\theta)}{\partial t} = \frac{1}{\pi a^2} \frac{\partial \theta_n(\theta)}{\partial \theta} \frac{\partial \theta}{\partial t} \quad (23b)$$

To proceed with the analytical derivations, similar to findings in the RSA simulations of a power law dependence of rate of change of θ with t , the following generalized parametric form is used:

$$\frac{\partial \theta}{\partial t} = k_1 t^\beta \quad (23c)$$

where k_1 is a constant with units of $s^{-1-\beta}$ and β is a dimensionless parameter characterizing the power law dependence of θ with t . Values for k_1 and β can be determined from first principles by multiparticle Brownian dynamics simulations, which are very time-consuming (extensive CPU time). In this work the values are determined by comparison to experimental observations that reflect the overall growth dynamics of the deposit (discussed in a later section in detail). Thus, the variation of θ with t is given by

$$\theta = \frac{k_1}{\beta + 1} t^{\beta+1} \quad (23d)$$

Combining eqs 23b and 23c

$$J_n(\theta) = \frac{k_1 t^\beta}{\pi a^2} \frac{\partial \theta_n(\theta)}{\partial \theta} \quad (23e)$$

Using expression for θ_n from eqs 18 and 19

$$J_{n=1}(\theta) = \frac{k_1 t^\beta}{\pi a^2} \frac{\partial}{\partial \theta} (\theta_1^{\max} - b \exp(-\gamma \theta)) = \left(\frac{k_1 t^\beta}{\pi a^2} \right) b \gamma \exp(-\gamma \theta) \quad (24)$$

and

$$J_{n \geq 2}(\theta) = \frac{k_1 t^\beta}{\pi a^2} \frac{\partial}{\partial \theta} \left(\frac{\theta_n^{\max}}{1 + \exp[-\varphi_n(\theta - \theta_n^0)]} \right) = \left(\frac{k_1 t^\beta}{\pi a^2} \right) \left(\frac{\varphi_n \theta_n^{\max}}{2} \right) \frac{1}{\cosh[-\varphi_n(\theta - \theta_n^0)] + 1} \quad (25)$$

An expression for available surface functions $\Phi_n(\theta)$ for each layer can now be obtained by combining eqs 24, 25, and 23a and noting that $J = k_{\text{dep}} C_0$. Hence

$$\Phi_{n=1}(\theta) = \frac{1}{k_{\text{dep}} C_0} \left(\frac{k_1 t^\beta}{\pi a^2} \right) b \gamma \exp(-\gamma \theta) \quad (26)$$

and

$$\Phi_{n \geq 2}(\theta) = \left(\frac{1}{k_{\text{dep}} C_0} \right) \left(\frac{k_1 t^\beta}{\pi a^2} \right) \left(\frac{\varphi_n \theta_n^{\max}}{2} \right) \frac{1}{\cosh[-\varphi_n(\theta - \theta_n^0)] + 1} \quad (27)$$

The right-hand side of eq 26 is a monotonically decreasing function with respect to θ , while that of eq 27 has a maximum at $\theta = \theta_n^0$. Equations 26 and 27 give the probability of particles depositing in the n th layer at time t for a given value of θ . It should be noted that the values of k_{dep} , C_0 , a , k_1 , and β should be known a priori to obtain the value of the available surface function. Figure 3a shows a plot of $\Phi_n(\theta)$ as a function of θ for the case of diffusional deposition in the absence of interactions (deposit in Figure 2a). The values of other parameters used were $k_{\text{dep}} = 10^{-7} \text{ m} \cdot \text{s}^{-1}$, $C_0 = 10^{16} \text{ m}^{-3}$, $\beta = 0.05$, $k_1 = 2.34 \times 10^{-6} \text{ s}^{-1.05}$, and $a = 30 \text{ nm}$. The figure shows

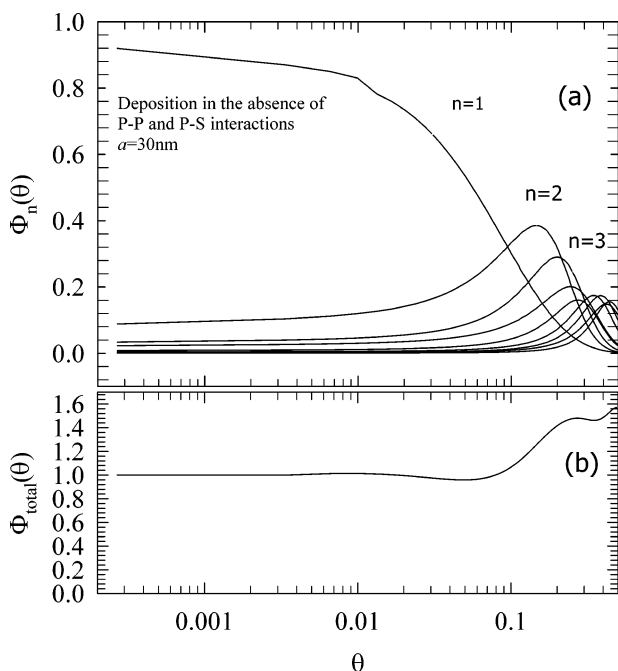


FIGURE 3. Variation as a function of θ of (a) available surface function in each layer Φ_n and (b) the total available surface function $\Phi_{\text{total}}(\theta)$. Simulations were for pure diffusional deposition (no P–P and P–S interactions considered)

that the probability of particle depositing on the surface ($n = 1$) initially ($\theta = 0$) is close to 1 (with very few particles depositing in the second layer) and then decreases monotonically approaching 0. In each upper layer ($n \geq 2$), the probability has a distribution, with maximum probability at a certain value of θ ($=\theta_n^0$). Φ_n , defined as in eqs 26 and 27, can thus be interpreted as a switching function that dictates at what values of θ each layer starts to fill and subsequently reaches saturation. It also determines the rate at which a layer is filled. As the coverage in the first layer begins to approach saturation coverage, the probability of deposition in that layer starts decreasing. At the same time, the probability of particles depositing in the second layer gradually starts increasing and reaches a maximum at a certain value of θ . A few particles concurrently deposit in the third and upper layers, although with low probabilities. As the coverage in the second layer begins to approach its saturation value, the probability of particles depositing in the second layer starts decreasing and that in the third (and upper) layer start increasing. Each layer thus goes through a similar phase of increasing and decreasing deposition. From eqs 26 and 27, the total available surface function for the entire deposit can now be written as

$$\Phi_{\text{total}}(\theta) = \frac{J}{J_0} = \frac{1}{k_{\text{dep}} C_0} \left(\frac{k_1 t^\beta}{\pi a^2} \right) \left(b \gamma \exp(-\gamma \theta) + \sum_{n=2}^N \left(\frac{\varphi_n \theta_n^{\max}}{2} \right) \frac{1}{\cosh[-\varphi_n(\theta - \theta_n^0)] + 1} \right) \quad (28)$$

Equation 28 gives the total available surface function for the deposit, and the entire kinetic information is embedded in it. The number of layers N over which the summation is carried out will depend on the stage of deposition. For instance, in the initial stage of deposition, particles deposit only in the first few layers ($n < 10$), and considering the first 10 layers will give a sufficiently accurate value of $\Phi_{\text{total}}(\theta)$. In this study, whenever feasible, the first 25 layers are considered to compute $\Phi_{\text{total}}(\theta)$.

It should be noted that available surface function as defined in eq 28 assumes that variation of coverage in each layer can be described using eqs 18 and 19. While this assumption is valid in most multilayer deposition systems since the expressions are obtained by fitting results from multilayer simulations, it fails to capture the dynamics of ideal hard-sphere monolayer systems. For an ideal hard-sphere deposition, the coverage on the deposition surface ($\theta_1(\theta)$) increases linearly with θ (with $(d\theta_1(\theta)/d\theta) = 1$) to reach saturation and cannot be described by eq 19. Wherever applicable, the RSA blocking function (eq 4b) has been used to describe dynamics of monolayer deposition in this study.

Figure 3b shows a plot of $\Phi_{\text{total}}(\theta)$ computed using eq 28 and is sum of all $\Phi_n(\theta)$ at a given θ in Figure 3a. Figure 3b shows that $\Phi_{\text{total}}(\theta)$ is 1 initially (i.e., the actual flux is equal to J_0 , nascent surface flux available from macroscopic transport). $\Phi_{\text{total}}(\theta)$ then gradually starts increasing due to increase in the surface area made available by the deposited particles. It should be noted that deposition flux is more than J_0 at all θ . If it is assumed that the entire spherical surface area of the deposited particles is available for deposition, then the total surface area available for deposition is approximately = (area of bare deposition surface) – (projected area covered by particles in the first layer) + (surface area of the particles in the first layer) + (surface area of the particles in the upper layers) $\approx 1 - \theta_1 + 2\theta_1 + 4(\theta - \theta_1) = 1 - 3\theta_1 + 4\theta$. Since in the initial stage of deposition, $\theta = \theta_1$, the available area can be approximated by $(1 + \theta)$. Thus the available area keeps increasing with θ for the case of

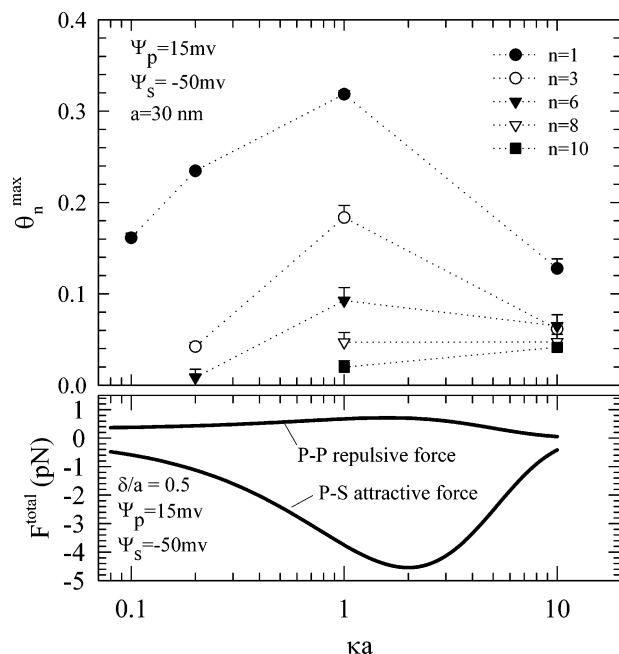


FIGURE 4. Variation as a function of κa of (a) saturation coverage in each layer and (b) P–P and P–S interaction forces. $\Psi_p = 15$ mV, $\Psi_s = -50$ mV, $a = 30$ nm, and $\delta/a = 0.5$, where δ is the surface-to-surface separation distance.

diffusional deposition in the absence of interactions. Since the available surface function only reflects change in available surface area in this case (i.e., when no interactions are present), it increases with increasing θ in Figure 3b. It should be noted that this trend in $\Phi_{\text{total}}(\theta)$ is in contrast to monolayer RSA available surface function, which monotonically decreases from 1 to 0, since available area for deposition also decreases with increasing θ .

Influence of Ionic Strength on Deposition Kinetics. The approach developed in the previous section can be used to study influence of ionic strength on the deposition kinetics. As the ionic strength (characterized by κa) of the medium changes, the range of electrostatic interactions between P–P and P–S also change, which further affect the kinetics of deposition. It should be pointed out that for low values of κa (≈ 0.1) electrostatic interactions are long ranged but weaker in magnitude. For larger κa values (≈ 10) the interactions are short ranged but stronger in magnitude. Figure 4a shows variation in saturation coverage in different layers ($n = 1, 3, 6, 8$, and 10) as a function of κa for a 30 nm particle at $\Psi_p = 15$ mV and $\Psi_s = -50$ mV. The coverages are averaged over six replicate simulations. Saturation coverages in all layers are significantly lower compared to the hard-sphere jamming limit of 0.545 due to influence of interparticle interactions. Maximum fractional coverage in the first layer (on the deposition surface, $n = 1$) increases from 0.16 at $\kappa a = 0.1$ to 0.23 at $\kappa a = 0.2$ and 0.32 at $\kappa a = 1$ and then starts decreasing with increasing κa . Coverages are maximum at $\kappa a = 1$. This increasing–decreasing trend is consistent with the variation of P–P and P–S forces with κa shown in Figure 4b. Figure 4b shows variation of total P–P and P–S force at a surface-to-surface separation distance of 0.5 (normalized by a) as a function of κa . Both P–P and P–S forces go through a maximum at $\kappa a \approx 2$. Correspondingly, coverages also go through a maximum at $\kappa a \approx 1$. The results are qualitatively similar to those reported by Kulkarni et al. (22) for a one-dimensional deposition surface. It should also be pointed out that deposition for $\kappa a = 0.1$ is almost monolayer (coverage at $n = 2$ is 0.025; not shown in Figure 4a) due to high lateral double layer repulsion. For $\kappa a = 0.2$, deposition stops after $n = 6$ due to large P–P repulsion forces contributed by

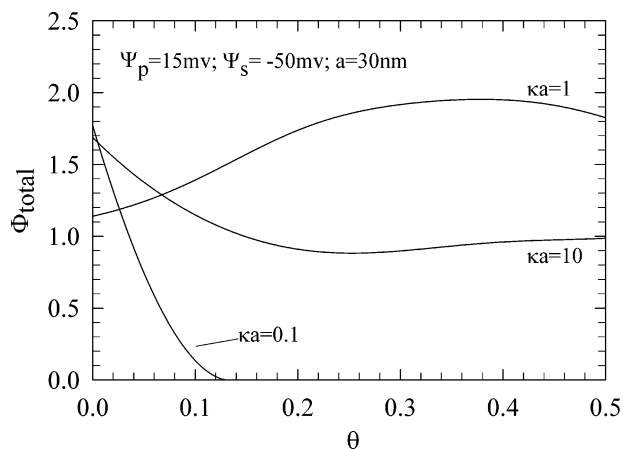


FIGURE 5. Variation of total available surface function ($\Phi_{\text{total}}(\theta)$) as a function of θ at different values of κa . $\Psi_p = 15$ mV, $\Psi_s = -50$ mV, $a = 30$ nm.

neighboring particles in the fractal deposit. For higher κa values, coverages are lower due to increased physical screening by the particles deposited in the upper layers.

Figure 5 shows the total available surface function ($\Phi_{\text{total}}(\theta)$) at three values of κa , for the corresponding case in Figure 4. The total available surface function was computed according to eq 28. Required parameters were obtained directly from the simulation. Values of other parameters used in the calculation were $k_{\text{dep}} = 10^{-7} \text{ m} \cdot \text{s}^{-1}$, $C_0 = 10^{16} \text{ m}^{-3}$, $\beta = 0.0$, $k_1 = 2.83 \times 10^{-6} \text{ s}^{-1.0}$, and $a = 30$ nm. A full-grown fractal structure was obtained from the simulations and variation of $\theta_n(\theta)$ with θ was then computed. Equations 19 (for the first layer) and 18 (layers 2 and above) were then fitted to these data to obtain required parameters in eq 28.

As seen in the Figure 5, deposition kinetics remarkably vary as the dimensionless Debye length (κa) changes from 0.1 to 10. At $\kappa a = 0.1$, the available surface function monotonically decreases from about 1.76 at $\theta = 0$ to 0 at $\theta = 0.13$ resembling the RSA-type blocking function in monolayer deposition. At this low ionic strength, interactions are long-ranged, and high repulsion from the deposited particles results in practically monolayer deposition with $\theta_{n=1}^{\max} = 0.16$, $\theta_{n=2}^{\max} = 0.025$, $\theta_{n=3}^{\max} = 0.0009$ (deposition stops after third layer). As κa is further increased to 1, interactions become short-ranged, and the magnitude of P–S attractive force dominates over the P–P repulsion, at this ionic strength (see Figure 4b). As a result, the deposition flux increases with increasing surface area of the deposit. As the ionic strength is further increased (i.e., as κa increases to 10), $\Phi_{\text{total}}(\theta)$ shows a completely different trend. At this ionic strength, P–P repulsive interactions dominate; P–P forces are long-ranged, although weak in magnitude. Accordingly, the flux initially decreases with increasing θ , and then starts increasing gradually due to increase in surface area made available by the deposited particles. Moreover, note that the values of available surface function (Φ_{total}) at $\theta \approx 0$ qualitatively follow a trend similar to that for the surface coverage ($\theta_{n=1}$) in Figure 4a; that is, Φ_{total} decreases as κa is increased from 0.1 to 10.

Predicting Macroscopic Flux in Porous Media. The approach developed above can be used to compute macroscopic deposition flux in porous media as outlined in Figure 1a. $\Phi_{\text{total}}(\theta)$ can be estimated from the simulations according to eq 28. All parameters on the right-hand side of eq 28 can be directly obtained from the Brownian dynamic simulations in this study, except the two parameters k_1 and β . These two parameters characterize kinetics of θ according to eq 23c. As described earlier, in this work a sequential algorithm was used that involved releasing particles one by one, such that a new particle is released into the simulation box only after

TABLE 3. Physicochemical Parameters Used in the Simulation, Corresponding to Experimental Data^a of Ref 1

parameter	$\kappa a = 1.1$	$\kappa a = 15.4$	$\kappa a = 34.3$
collector radius, a_c (μm)	55	55	55
particle diffusion coefficient, D ($\text{m}^2\cdot\text{s}^{-1}$)	7.4×10^{-12}	7.4×10^{-12}	7.4×10^{-12}
particle radius, a (nm)	33	33	33
depth of packed column, L (cm)	1.3	1.3	1.3
superficial fluid velocity, V_s ($\text{m}\cdot\text{s}^{-1}$)	1.76×10^{-4}	1.76×10^{-4}	1.76×10^{-4}
particle number concentration, C_0 (m^{-3})	2.1×10^{16}	2.1×10^{16}	2.1×10^{16}
particle transfer coefficient, k_{dep} ($\text{m}\cdot\text{s}^{-1}$)	1.2×10^{-6}	8.68×10^{-7}	5.5×10^{-7}
constant, k_1 (eq 23c) ($\text{s}^{-1-\beta}$)	-	8.04×10^{-5}	1.39×10^{-5}
power, β (eq 23c)	-	-0.05	0.315
ionic strength of medium, I ($\text{mol}\cdot\text{L}^{-1}$)	1.0×10^{-4}	2.0×10^{-2}	1.0×10^{-1}
particle potential, Ψ_p (mV)	76	46	31
deposition surface potential, Ψ_s (mV)	-74	-48	-22

^a Experimental data corresponding to deposition of hematite particles on glass, dispersed in aqueous solutions. Other parameters used were as follows: media porosity = 0.36; particle diffusivity = $7.4 \times 10^{-12} \text{ m}^2\cdot\text{s}^{-1}$; particle density = $5.24 \text{ g}\cdot\text{cm}^{-3}$; density of water = $0.997 \text{ g}\cdot\text{cm}^{-3}$; dynamic viscosity of water = $8.9 \times 10^{-4} \text{ Pa}\cdot\text{s}$; Hamaker constant for P-S interaction = 10^{-20} J ; Hamaker constant for P-P interaction = 10^{-20} J .

the previously released particle deposited. This algorithm tracks the total time taken by each particle to deposit but does not involve an actual, chronological time scale (t) that can be used to relate θ with t . In the absence of this information from first principles, the approach developed above can be used to extract information about the morphological evolution of particle deposit at the collector surface from an experimental particle breakthrough curve. The approach involves treating k_1 and β as fitting parameters and solving eqs 2a and 2b along with eq 28 to match the experimental breakthrough curves. Multiparticle Brownian dynamic simulations can be performed to evaluate these constants (parameters k_1 and β) from first principles, although at the expense of significantly increasing the CPU time requirements. This is beyond the scope of the present study where the primary goal is to validate the novel approach described.

Once values for parameters k_1 and β are available, the multiscale linking approach was validated using experimental breakthrough curves reported by Ryde et al. (1). Multilayer deposition of spherical hematite particles ($a = 33 \text{ nm}$) onto spherical glass collectors ($a_c = 55 \mu\text{m}$) in a 1.3 cm deep packed column was used to obtain particle breakthrough curves. Simulations were performed under identical conditions to obtain Φ_{total} for the experimental system of Ryde et al. (1) with physical and chemical parameters as listed in Table 3. Particle and surface potentials were approximated by measured electrokinetic potentials. Figure 6a,b shows experimental and predicted particle breakthrough curves at three ionic strengths (I) of 1×10^{-4} , 2×10^{-2} , and 10^{-1} M corresponding to $\kappa a \approx 1.1$, 15.4, and 34.3, respectively. Though k_1 and β have been used as adjustable parameters to obtain better quantitative agreement, their definitions have a clear physical meaning (they together define how θ varies with time t). Values of k_{dep} (i.e., particle transfer coefficient for clean collector surface) were estimated using eq 2 to match the first experimental data point. It is worth noting that values of k_{dep} can be theoretically estimated with reasonable accuracy for given physicochemical and hydrodynamic conditions (30).

Figures 6a,b show good agreement between the predicted (solid lines) and experimental (symbols) values, particularly at high ionic strength (Figure 6b). Figure 6a ($\kappa a = 1.1$) corresponds to monolayer deposition due to high lateral repulsion between deposited particles. Accordingly, the monolayer RSA dynamical blocking function (eq 4b) was used along with the monolayer saturation coverage predicted by the simulations to obtain the breakthrough curve. As noted earlier, for strictly monolayer deposition with high interparticle repulsive interaction, variation of coverage on the surface (θ_1) increases linearly with θ and cannot be described

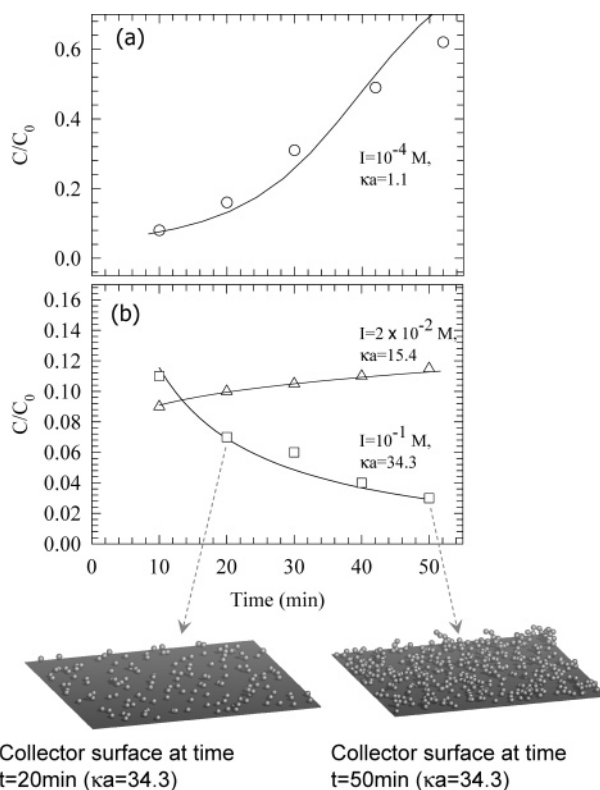


FIGURE 6. Experimental data of Ryde et al. (1) (symbols) for irreversible deposition of spherical hematite particles on glass surfaces in aqueous dispersion at three ionic strengths. Physical and chemical parameters of the system are listed in Table 4. Predicted values from this work are shown by solid lines. Deposition at low ionic strength ($I = 10^{-4}$) was clearly monolayer; predicted curve is based on RSA-type available surface function (eq 4b). The nominal inlet particle concentration was close to $2.1 \times 10^{16} \text{ m}^{-3}$ in the experiments (1). Other parameters used in computation are listed in Table 4. Also shown are the snapshots of collector surface at the column entrance ($Z = 0 \text{ cm}$) at time $t = 20$ and 50 min. The deposits clearly show multilayered structures at long times.

using eq 19. The predicted breakthrough concentration is slightly higher at long times compared to experimental values. Potentials based on linear superposition approximation have been known to overestimate the interactions at close separations (31). Thus, the maximum coverage predicted by the simulations at $\kappa a = 1.1$ could be smaller than the corresponding experimental value. The agreement in Figure 6b at $\kappa a = 15.4$ and $\kappa a = 34.3$ is remarkable, considering the fact that the potentials used to represent P-P and P-S

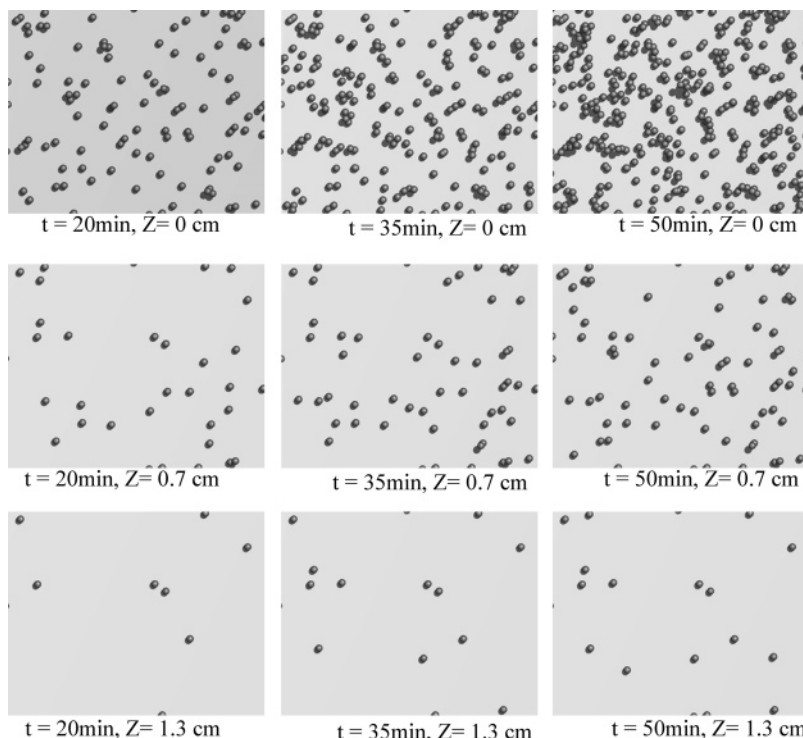


FIGURE 7. Snapshots of collector surface obtained from the simulations at column entrance ($Z = 0$ cm), midway between the column ($Z = 0.7$ cm), and column exit ($Z = 1.3$ cm) at different times. Corresponding to simulation curve in Figure 6b at $\kappa a = 34.3$.

interactions are only approximate at best. The qualitative trend of increasing deposition with time (“ripening”) at $\kappa a = 34.3$ is captured by the model. Figure 6b also shows snapshots of collector surface located at the column entrance ($Z = 0$ cm) obtained from the simulations at time $t = 20$ and 50 min for $\kappa a = 34.3$. The deposit had a multilayered structure at long times.

Figure 7 shows the top view of collector surfaces (obtained from simulation) at different locations in the column (entrance, middle, and exit) as the deposition progresses for the case of $\kappa a = 34.3$ in Figure 6b. As expected, the number density of deposited particles decreases as the distance from the column entrance increases. At any given location in the column, the number density increases with time. At long times the deposition is clearly multilayered.

Values of parameters k_1 and β were obtained by trial and error to get the best quantitative agreement with the experimental data. As noted earlier, the approach used in this work requires that the values of k_1 and β be known a priori. k_1 is a proportionality constant ($k_1 \sim O(\pi a^2 k_{\text{dep}} C_0)$, since $\Phi_{\text{total}} \sim O(1)$), whereas, exponent β influences the transient features of deposition. While kinetics of monolayer systems are well studied and time dependence of θ is known, no such information is available for a multilayered system. The different values of β obtained for curves in Figure 6b ($\beta = -0.05$ at $\kappa a = 15.4$ and $\beta = 0.315$ at $\kappa a = 34.3$) suggest that dynamics of multilayered systems could be significantly different from that of ideal monolayer systems.

A mechanistic framework that integrates basic understanding of the physicochemical phenomena at the mesoscale with the continuum-level transport equations was used to obtain meaningful results for systems involving particle deposition. With values of two parameters that describe overall deposition kinetics determined from experiments, the detailed dynamics of deposition was predicted, and the influence of solution ionic strength was successfully investigated. The approach can be generalized and extended to predict the influence of other parameters such as particle and collector radius, surface charge heterogeneity, and

hydrodynamic interactions on particle deposition in practical systems such as deep bed filters. A 2-fold approach can be taken for determining the overall deposition kinetic parameters—one, as presented in this work, from experiments for a specific type of system; or second, using rigorous, computationally intensive first principles multiparticle Brownian dynamics simulations.

Acknowledgments

P.K. acknowledges partial support by a Henry Schwartz, Jr., scholarship from the School of Engineering and Applied Science, Washington University in Saint Louis. Malcolm Tobias of the Center for Scientific and Parallel Computing at Washington University in Saint Louis is thanked for assistance with implementation of the computing algorithm. The CPU allocation provided by National Computational Science Alliance at the University of Illinois is also gratefully acknowledged.

Literature Cited

- (1) Ryde, N.; Kihira, H.; Matijevic, E. Particle adhesion in model systems: 15. Effect of colloid stability in multilayer deposition. *J. Colloid Interface Sci.* **1992**, *151* (2), 421–432.
- (2) Schaaf, P.; Voegel, J.-C. From random sequential adsorption to ballistic deposition: a general view of irreversible deposition processes. *J. Phys. Chem. B* **2000**, *104*, 2204–2214.
- (3) Adamczyk, Z.; Belouschek, P. Localized adsorption of particles on spherical and cylindrical interfaces. *J. Colloid Interface Sci.* **1991**, *146* (1), 123–136.
- (4) Adamczyk, Z.; Siwek, B.; Zembala, M.; Belouschek, P. Kinetics of localized adsorption of colloidal particles. *Adv. Colloid Interface Sci.* **1994**, *48*, 151–280.
- (5) Adamczyk, Z. Kinetics of diffusion-controlled adsorption of colloid particles and proteins. *J. Colloid Interface Sci.* **2000**, *229*, 477–489.
- (6) Johnson, C. A.; Lenhoff, A. M. Adsorption of charged latex particles on mica studied by atomic force microscopy. *J. Colloid Interface Sci.* **1996**, *179*, 587–599.
- (7) Johnson, P. R.; Elimelech, M. Dynamics of colloid deposition in porous-media—blocking based on random sequential adsorption. *Langmuir* **1995**, *11*, 801–812.

- (8) Schaaf, P.; Vogel, J.-C.; Senger, B. Irreversible deposition/adsorption processes on solid surfaces. *Ann. Phys. Fr.* **1998**, 23(6), 1–89.
- (9) Hinrichsen, E. L.; Feder, J.; Jossang, T. Geometry of random sequential adsorption. *J. Stat. Phys.* **1986**, 44 (5–6), 793–827.
- (10) Feder, J. Random sequential adsorption. *J. Theor. Biol.* **1980**, 87 (87), 237.
- (11) Adamczyk, Z.; Weroni, P.; Musial, E. Colloid particle adsorption on partially covered (random) surfaces. *J. Colloid Interface Sci.* **2001**, 241 (1), 63–70.
- (12) Wojtaszczyk, P.; Schaaf, P.; Senger, B.; Zembala, M.; Voegel, J. C. Statistical properties of surfaces covered by large spheres. *J. Chem. Phys.* **1993**, 99 (9), 7198–7208.
- (13) O'Melia, C. R.; Ali, W. Role of retained particles in deep bed filtration. *Prog. Water Technol.* **1978**, 10, 167.
- (14) Tien, C. *Granular Filtration of Aerosols and Hydrosols*; Butterworth Publishers: Woburn, MA, 1989.
- (15) Song, L.; Elimelech, M. Dynamics of colloid deposition in porous media: modelling the role of retained particles. *Colloids Surf.* **1993**, 73, 49.
- (16) Liu, D.; Johnson, P.; Elimelech, M. Colloid deposition dynamics in flow through porous media: role of electrolyte concentration. *Environ. Sci. Technol.* **1995**, 29, 2963–2973.
- (17) Privman, V.; Frisch, H. L.; Ryde, N.; Matijevic, E. Particle adhesion in model systems. Part 13. Theory of multilayer deposition. *J. Chem. Soc., Faraday Trans.* **1991**, 87 (9), 1371.
- (18) Lubachevsky, B. D.; Privman, V.; Roy, S. C. Morphology of amorphous layers ballistically deposited on a planar substrate. *Phys. Rev. E* **1993**, 47, 48–53.
- (19) Wiesner, M. R. Morphology of particle deposits. *J. Environ. Eng. ASCE* **1999**, 125 (12), 1124–1132.
- (20) Veerapaneni, S.; Wiesner, M. R. Deposit morphology and head loss development in porous media. *Environ. Sci. Technol.* **1997**, 31 (10), 2738–2744.
- (21) Tarabara, V. V.; Pierrisnard, F.; Parron, C.; Bottero, J. Y.; Wiesner, M. R. Morphology of deposits formed from chemically heterogeneous suspensions: Application to membrane filtration. *J. Colloid Interface Sci.* **2002**, 256 (2), 367–377.
- (22) Kulkarni, P.; Sureshkumar, R.; Biswas, P. Multiscale simulation of irreversible deposition in the presence of double layer interactions. *J. Colloid Interface Sci.* **2003**, 260 (1), 36–48.
- (23) Kuhnien, F.; Barmettler, K.; Bhattacharjee S.; Elimelech M.; Kretzschmar, R. Transport of iron oxide colloids in packed quartz sand media: monolayer and multilayer deposition. *J. Colloid Interface Sci.* **2000**, 231, 32–41.
- (24) Schaaf, P.; Talbot, J. Surface exclusion effects in adsorption processes. *J. Chem. Phys.* **1989**, 91 (7), 4401–4409.
- (25) Adamczyk, Z.; Siwek, B.; Zembala, M. Reversible and irreversible adsorption of particles on homogeneous surfaces. *Colloids Surf.* **1992**, 62 (1–2), 119–130.
- (26) Ermak, D. L.; Yeh, Y. Equilibrium electrostatic effects on behavior of polyions in solution: polyion-mobile ion interaction. *Chem. Phys. Lett.* **1974**, 24, 243–248.
- (27) Ermak, D. L. Computer simulation of charged particles in solution. I. Technique and equilibrium properties. *J. Chem. Phys.* **1975**, 62, 4189–4196.
- (28) Ansell, G. C.; Dickinson, E. Sediment formation by Brownian dynamics simulation: Effect of colloidal and hydrodynamic interaction on sediment structure. *J. Chem. Phys.* **1986**, 85 (7), 4079–4086.
- (29) Meakin, P. Diffusion-controlled deposition on surfaces: Cluster-size distribution, interface exponent, and other properties. *Phys. Rev. B* **1984**, 30 (8), 4207–4214.
- (30) Elimelech, M. Particle deposition on ideal collectors from flowing suspensions: Mathematical formulation, numerical solution, and simulations. *Sep. Technol.* **1994**, 4, 186–212.
- (31) Adamczyk, A.; Weroni, P. Application of the DLVO theory for particle deposition problems. *Adv. Colloid Interface Sci.* **1999**, 83, 137–226.
- (32) Magan R. V.; Sureshkumar R. A multiscale-linking algorithm for the simulation of irreversible deposition. *Multiscale Model. Simul.* **2004**, 2, 475–500.
- (33) Sader J. E. Accurate analytic formulae for the far field effective potential and surface charge density of a uniformly charged sphere. *J. Colloid Interface Sci.* **1997**, 188 (2), 508–510.

Received for review January 11, 2005. Revised manuscript received April 17, 2005. Accepted April 24, 2005.

ES0500557